1   **REVISION 2**

2

3   **Kinetics of Fe(III) mineral crystallization from ferrihydrite in the presence of Si at alkaline**

4   **conditions**

5   **Paul Clarence M. Francisco[1]*, Tsutomu Sato[1]*, Tsubasa Otake[1], Takeshi Kasama[2]**

6   [1]Environmental Geology Laboratory, Division of Sustainable Resources Engineering,

7   Faculty of Engineering, Hokkaido University, Kita 13 Nishi 8, Sapporo, 060-8628, Japan

8   [2]Center for Electron Nanoscopy, Technical University of Denmark,

9   DK-2800 Kongens Lyngby, Denmark

10   *correspondence: paulcmfrancisco@frontier.hokudai.ac.jp; tomsato@eng.hokudai.ac.jp

11

12   **ABSTRACT**

13   Fe(III) minerals are ubiquitous in diverse near-surface environments, where they exert

14   important controls on trace species transport. In alkaline environments such as the glass-steel

15   interface in geological high-level radioactive waste disposal sites that use cement for plugging and

16   grouting, Fe minerals are closely associated with Si that may affect their crystallization behavior as

17   well as their capacities to regulate hazardous element cycling. While it is well-known that Si retards

18   Fe mineral crystallization, there is currently an overall lack of quantitative information on the rates

19   of crystallization of stable Fe minerals in the presence of Si at alkaline conditions. Crystallization of

20   Fe(III) minerals goethite and hematite from ferrihydrite co-precipitated with different amounts of Si

21   was studied at pH 10 and at temperatures ranging from 50 to 80°C using powder x-ray diffraction

22   (XRD) and transmission electron microscopy (TEM). Mineral abundances evaluated from Rietveld

23   refinement of XRD data show that the proportion of goethite in the final assemblage decreases

24   relative to hematite with increasing Si. TEM observation of goethite and hematite crystals formed in

25   the presence of Si show significant morphological differences compared to those formed in the

26   absence of Si. Rate constants for crystallization derived from fitting of time-dependent changes in

1

27   mineral abundances with the Avrami equation show a decreasing trend with increasing Si for both

28   goethite and hematite. Apparent activation energies for crystallization for both minerals increase

29   with increasing Si, with that of goethite increasing more drastically compared to hematite,

30   indicating the inhibitive effect of Si on the crystallization of both minerals. The overall inhibition of

31   crystallization may be explained in terms of the effects of Si on the surface properties of the

32   ferrihydrite precursor. The rate constants and apparent activation energies reported in this study

33   may be useful in estimating the crystallization behavior and timescales of Fe minerals in both

34   natural and engineered environments. These informations may eventually be helpful in predicting

35   the fate of hazardous elements in such environments.

36   *Keywords: ferrihydrite, goethite, hematite, silica, crystallization kinetics, activation energy*

37

38   **Introduction**

39   Fe(III) hydroxide and oxide phases such as goethite (α-FeOOH) and hematite (α-Fe$_2$O$_3$) are

40   widely distributed in different natural (e.g. soils, sediments) and engineered environments (e.g.

41   geological waste disposal, water treatment technologies). Due to their high surface areas and

42   surface reactivity, these phases have excellent sorption capacities for anions (e.g. sulfate, phosphate,

43   arsenate, etc.), metals (e.g. Pb, Cu, Ni) as well as organic compounds, exerting significant controls

44   on the transport and availability of these substances (Cornell and Schwertmann, 2003).

45   In engineered environments such as deep geological repositories for high-level nuclear

46   wastes, initially reducing conditions may eventually give way to more oxidizing conditions in the

47   long-term due to influx of oxygenated groundwater. In such cases, poorly ordered Fe(II,III)

48   hydroxysalts, ferrihydrite, goethite and hematite are among a suite of corrosion products expected

49   to form during aqueous corrosion of important steel components of the repository, such as the steel

50   overpack (Refait et al., 2003; Kwon et al., 2007; Hazan et al., 2013). In Japanese disposal concepts,

51   the use of cement as structural liners for tunnels, as mechanical support for the backfill and as

52   grouting material for fractures arising from the country's active geologic setting (NUMO, 2004b) is

53   expected to generate alkaline fluids around the repository. A breach in the canister, coupled with the

54   presence of alkaline fluids, could result in the dissolution of vitrified waste and the release of high-

55   yield radionuclides (e.g. U, Se, Tc) into the wider environment. Formation of Fe(III) phases from

56   steel corrosion, however, may provide a sink for these elements, which exist as oxyanions, via

57   adsorption and/or co-precipitation (e.g. Bargar et al., 1999; Rovira et al., 2008; Marshall et al.,

58   2014). In particular, ferrihydrite, a poorly ordered Fe-oxyhydroxide that forms by the hydrolysis of

59   Fe(II) and Fe(III) ions (Cudennec and Lecerf, 2006; Dyer et al, 2010), has exhibited superior

60   sorption properties for these elements due to its high specific surface area (Das et al., 2013). In

61   aqueous systems, oxide phases such as goethite and hematite typically crystallize via the

62   transformation of the metastable and poorly ordered intermediate phase ferrihydrite. Crystallization

63   of goethite and hematite, however, may potentially modify the ability of corrosion products to

64   scavenge hazardous metals from solution due to differences in surface area and reactivity (Buekers

65   et al., 2008; Bazilevskaya et al., 2012).

66   The crystallization mechanisms of goethite and hematite from ferrihydrite in aqueous systems

67   involve mutually exclusive and competitive processes that depend on parameters such as pH and

68   temperature. Goethite forms through direct nucleation from aqueous solutions following the

69   dissolution of the ferrihydrite precursor. Under high pH conditions (pH > 10), this crystallization

70   mechanism is pronounced due to the increased solubility of the ferrihydrite precursor and the high

71   concentration of $Fe(OH)_4^-$ species favorable for goethite crystal growth (Schwertmann and Murad,

72   1983). On the other hand, hematite crystallization proceeds by the aggregation, dehydration and

73   solid-state transformation of ferrihydrite particles. This transformation pathway is promoted at

74   higher temperatures, which favor dehydration and at near neutral to mildly alkaline (pH < 10)

75   conditions, under which ferrihydrite particles tend to aggregate (Cudennec and Lecerf, 2006).

76   The kinetics of crystallization of goethite and hematite from ferrihydrite at alkaline

77   conditions and in the absence of foreign compounds has been investigated extensively, such that

78   there is abundant quantitative data available. Data obtained from studies on Fe-oxide color change

3

79   at 40°C to 85°C show that apparent activation energies for goethite crystallization are 56.1 kJ/mol

80   and 48.2 kJ/mol at pH 11.7 and 12.2, respectively (Nagano et al., 1994). More recent in-situ

81   crystallization experiments at pH 13.7 under a broader range of temperatures (60°C to 132°C)

82   obtained a value of 39 kJ/mol (Shaw et al., 2005). These kinetic data show that goethite

83   crystallization is favored by increasing pH. For hematite, the availability of kinetic data across a

84   broad pH range is more limited. Data obtained using phase quantification at pH 10 and at 25°C to

85   100°C estimate the apparent activation energy for hematite crystallization at 65 kJ/mol (Das et al.,

86   2011a) while in-situ crystallization experiments at pH 10.7 and at 72°C to 137°C give a value of 69

87   kJ/mol (Shaw et al., 2005).

88   However, at the interface of the corroding steel and dissolving glass, dissolved Si may co-

89   precipitate with and/or adsorb onto immediate corrosion products such as ferrihydrite. Early

90   investigations have recognized that Si alters the transformation rates of ferrihydrite. Studies on

91   solids formed from the oxidation of Fe(II) in solution showed that Si inhibited the formation of

92   crystalline lepidocrocite and favored the formation of ferrihydrite (Schwertmann and Thalmann,

93   1976). Solubility studies showed that ferrihydrite formed in the presence of Si has decreased

94   solubility in oxalate, suggesting that Si stabilizes ferrihydrite (Karim, 1984). These findings are

95   consistent with more systematic kinetic studies that showed the degree of transformation of

96   ferrihydrite to crystalline goethite, which is represented by the ratio of oxalate extractable Fe to the

97   total Fe (Fe_o/Fe_t), decreases with increasing Si (Cornell et al., 1987). The mechanism of inhibition is

98   generally thought to be the deposition of Si on the surfaces of ferrihydrite (Cornell et al., 1987;

99   Vempati and Loeppert, 1989; Doelsch et al., 2001; Swedlund et al., 2009; Dyer et al., 2010), which

100 may render ferrihydrite particles less soluble and less susceptible to aggregation. These studies

101 collectively show that Si inhibits the transformation of ferrihydrite and delays the crystallization of

102 more stable phases, potentially providing a long-term stable sink for radioactive elements released

103 from the glass. While the qualitative effect of Si on the formation of crystalline Fe(III) phases is

104 well known, there is however, paucity in quantitative kinetic data that may be useful in formulating

105   predictive models and building a robust safety case for high-level radioactive waste (HLW)

106   repositories.

107   The goal of this study is to obtain quantitative kinetic data for the crystallization of goethite

108   and hematite as a function of Si co-precipitated with Fe(III) at alkaline conditions and relate them

109   with their known formation mechanisms. In this study, we conduct the experiments at pH 10 for

110   two main reasons. First, the use of bentonite in Japanese designs as backfill between the overpack

111   and the host rock (JNC, 2000; NUMO, 2004a) may buffer the pH of potential hyperalkaline fluids

112   that may interact with the glass and steel to approximately 9 to 10 (Savage et al., 2002). Second, at

113   pH 10 the solubility of silica begins to increase (Stumm and Morgan, 1996), such that the effects of

114   Si on Fe(III) crystallization cannot be discounted. In addition, we also conduct the experiments in

115   the presence of nitrates, as nitrates are principal components in Japanese groundwaters (Kumazawa,

116   2002). Furthermore, nitrates are also present in significant amounts in disposal systems for other

117   waste classes such as trans-uranic (TRU) wastes (JAEA, 2007). While data obtained in this study is

118   useful for developing safety cases for nuclear waste repositories, insights into the mechanisms

119   involved may also be used to understand the effect of Si in natural environments.

120

121   **Materials and Methods**

122   **I. Synthesis**

123

124   Fe(III)) solution was prepared by dissolving reagent grade $Fe(NO_3)_3 \cdot 9H_2O$ (Kanto, 99%) in

125   ultrapure water (18 M Ω •cm) to create a 0.05 mol/L solution. Appropriate amounts of

126   tetraethylorthosilicate (TEOS; Alfa Aesar, 98%) were then added to the Fe solution to achieve Si

127   concentrations of 0 (Si/Fe = 0) to 1.25×10^{-3} mol/L (Si/Fe = 0.025). Preliminary experiments using

128   a broader range of Si concentrations showed that crystallization of goethite and hematite only

129   proceeded at timescales short enough to be investigated in the laboratory at these Si concentrations.

5

130   The Si-Fe mixture was stirred for about 30 minutes to dissolve the TEOS completely before

131   pH adjustment. The initial pH of the mixture was about 1.8, which was then adjusted to about

132   10.0±0.1 by titrating the solution with NaOH (Kanto, 97%). Addition of base hydrolyzed the Fe(III)

133   in solution, forming dark brown precipitates. The slurries were stirred for an additional 15 minutes

134   to allow the pH to stabilize. The slurries were then equally divided into 50 mL polypropylene

135   bottles and then stored at ovens preheated to 50, 60, 70 and 80°C to induce crystallization. Samples

136   extracted at different reaction durations were washed with deionized water to remove the salts and

137   freeze-dried for at least 24 hours. Selected samples from different temperatures and Si

138   concentrations were replicated to check the reproducibility of the results.

139

140   **II. Characterization of Synthetic Products**

141

142   Samples were analyzed by powder x-ray diffraction (XRD) using a Rigaku RINT2000 x-ray

143   diffractometer operating at 40 kV and 40 mA, equipped with a Cu target and graphite

144   monochromator. Samples were mixed with approximately 20 wt. % α-Al$_2$O$_3$ (Baikowski, CR-1

145   grade; crystallinity: 85%) to serve as an internal standard for phase quantification. The mixtures

146   were finely ground to minimize micro-absorption effects. Diffraction profiles were collected from

147   10 to 70° 2θ.

148   FTIR spectra were collected from 400 to 4000 cm^{-1} on a JASCO FTIR-4100 spectrometer

149   with 1.0 cm^{-1} spectral resolution. Pellets were prepared by mixing and crushing the samples with

150   KBr at a 1.5 mg sample: 250 mg KBr ratio. The KBr used to prepare the samples was heated at

151   110°C for two hours prior to use to remove the water.

152   To determine the zeta potential of the initial precipitates at pH 10, powders of fresh

153   precipitates were dispersed in a NaNO$_3$ medium set at pH 10 and an ionic strength of approximately

154   0.15 M, which is similar to the ionic strength of the parent solution from which they were

155   precipitated. The dilute precipitates are then transferred to a clear folded capillary cell and analyzed

6

156   using a Malvern Zetasizer Nano-ZS90. The values reported in this study are taken as the average of

157   up to 20 measurements, each consisting of 100 runs.

158   Selected samples were characterized using an FEI 80-300ST Titan transmission electron

159   microscope (TEM) operated at 300 kV, in order to study the morphology of individual mineral

160   particles. The lightly crushed samples were placed directly onto Cu TEM grids and mounted on a

161   low-background beryllium TEM specimen holder. Annular dark-field (ADF) imaging and energy

162   dispersive x-ray spectroscopic (EDS) elemental mapping was performed in scanning TEM mode

163   using an Oxford X-Max^{N} silicon drift detector equipped to the TEM. Each EDS spectrum was

164   acquired with a dwell time of 3 seconds in steps of 15 nm and was processed by principal

165   component analysis and pixel-by-pixel background subtraction (Kasama et al., 2015).

166

167   **III. Quantification of Fe(III) Phases**

168

169   To determine the proportion of phases in the samples, powder XRD data were refined by the

170   Rietveld refinement method using the commercial SIROQUANT program (Taylor and Clapp, 1992).

171   Rietveld refinement uses a non-linear least squares fitting approach to minimize the difference

172   between observed and calculated XRD patterns. The parameters refined for this study include the

173   half-width parameters, instrument zero, unit-cell parameters, asymmetry factors and the influence of

174   preferred orientation and corrections were applied to account for the absorption contrast between α

175   -Al_2O_3 and Fe-oxides. The quality of Rietveld refinement was evaluated from the values of χ^2 and R

176   factor given by the results of the fitting.

177   The ferrihydrite content of the sample cannot be directly determined from Rietveld

178   refinement due to its poorly crystalline nature. Treating it as an amorphous phase, its proportion

179   was estimated using the internal standard method, where the proportion of an amorphous phase is

180   related to the overestimation of the known internal standard, in this case α-Al_2O_3, defined by:

7

181
$$Fh(\%) = \frac{100}{100 - W_s}\left\{100\left(1 - \frac{W_s}{R_s}\right)\right\} \quad (1)$$

182   where W_s (%) is the weighted percentage of the internal standard and R_s (%) is its Rietveld

183   measured percentage (De la Torre et al., 2001; Westphal et al., 2009). To account for the presence

184   of an amorphous fraction in the internal standard, a modified form of Equation (1) is given by:

185
$$Fh(\%) = \frac{100}{100 - W_s}\left\{100\left(1 - \frac{W_{s,ct}}{R_s}\right) - W_{s,am}\right\} \quad (2)$$

186   where $W_{s,ct}$ (%) is the crystalline weight fraction of the standard, while $W_{s,am}$ (%) is its amorphous

187   weight fraction, was used. The uncertainty of the derived amorphous content was estimated from

188   the uncertainty given by the Rietveld refinement multiplied by the slope of Equation (2) (Westphal

189   et al, 2009).

190

191   **IV. Kinetic Analysis**

192

193   The weighted percentages of each phase over time derived from the Rietveld refinements

194   were normalized with the maximum percentage observed for a particular system to derive the

195   degree of reaction, α, given by the following equation:

196
$$\alpha = \frac{X_t}{X_{max}} \quad (3)$$

197   where X_t is the percentage at time t and X_{max} is the maximum percentage. The normalized data,

198   plotted as function of time, were fitted with the general form of the Johnson-Mehl-Avrami-

199   Kolmogorov (JMAK) model given by the equation (Avrami, 1939; 1940; 1941):

200
$$\alpha = 1 - e^{-k(t-t_0)^n} \quad (4)$$

201   where k is the rate constant (hr^{-1}), t is the time (hr), t_0 is the induction time and n is a parameter

202   related to the dimensionality and mechanism of growth. The parameters k, t_0 and n were used as

203   fitting parameters. The JMAK model has been previously utilized to describe crystallization

8

204   reactions of proteins (e.g. Li and Nail, 2005), solid-solid transformation (e.g. Houston et al., 2009)

205   and nucleation and growth (e.g. Shaw et al., 2005; Davidson et al., 2008)

206   Using data from experiments conducted at different temperatures, apparent activation

207   energies of crystallization for each system were derived from the Arrhenius equation, given by:

208
$$\ln k = -\frac{E_{a(cryst)}}{RT} + \ln A \quad (5)$$

209   where $E_{a(cryst)}$ is the apparent activation energy for crystallization (kJ/mol), R is the gas constant

210   (8.314×10^{-3} kJ/mol•K), T is the absolute temperature (K) and A is the pre-exponential factor (hr^{-1}).

211   The apparent activation energies provide information about crystallization mechanisms.

212

213   **Results**

214   **I. Characterization of Initial Precipitates**

215

216   **XRD.** Regardless of Si/Fe, XRD analyses of the initial dark brown precipitates extracted

217   before heating are characterized by two broad maxima centered at approximately 35° and 62° 2θ

218   (Fig. 1), which are consistent with 2-line ferrihydrite. No significant shift or changes in the width of

219   the ferrihydrite 'peaks' were observed in the range of Si concentration studied.

220   **FTIR Spectroscopy.** Infrared spectra for freshly precipitated solids extracted prior to

221   heating are generally consistent with published data on ferrihydrite (Russell, 1979; Cornell and

222   Schwertmann, 2003). Four distinct regions can be identified in the spectra (Fig. 2). First, the area

223   from ~2400 to ~3500 cm^{-1}, dominated by a broad absorption band with a maximum at

224   approximately ~3200 to ~3300 cm^{-1} corresponding to bulk OH stretching vibrations. The relatively

225   high background, which masks other vibrations in this region, is attributed to strong IR scattering

226   from small ferrihydrite crystallites (Vaughan et al., 2012). Second, the area from ~1300 to 1700 cm^{-}

227   ^{1}, where relatively sharp absorption bands at ~1350, ~1480 and ~1650 cm^{-1} corresponding to the

228   vibrations of adsorbed water are observed. From ~800 to ~1200 cm^{-1}, T-O-T and T-O stretching

229   vibrations can be observed. The low frequency region between 400 to ~700 cm^{-1} is characterized by

9

230   Fe-O stretching vibrations, O-T-O bending vibrations and bulk OH bending vibrations (Doelsch et

231   al., 2003).

232   The most significant changes with increasing Si concentration are observed in the third

233   region, where a relatively sharp band at ~930 cm^{-1} corresponding to asymmetric stretching

234   vibrations of Si-O-Fe bonds appears and increases in intensity with increasing concentration of Si.

235   At Si/Fe = 0.025, a shoulder at ~1060 cm^{-1} is observed, suggesting the presence of a small amount

236   of polymeric Si (Swedlund et al., 2010).

237   **Zeta Potential.** At pH 10, initial precipitates exhibit negative surface charge due to the

238   presence of hydroxyl groups on particle surfaces. With increasing Si, the surface charge on the

239   initial precipitates becomes more negative (Fig. 3). The silica-free precipitates have a zeta potential

240   of approximately -16.6 mV. This decreases to approximately -21.0 mV at Si/Fe = 0.025.

241

242   **II. Crystallization Experiments**

243

244   During heating of the ferrihydrite slurry, the initial precipitates undergo transformation to

245   the crystalline goethite (α-FeOOH) and hematite (α-Fe$_2$O$_3$) as indicated by distinct color changes

246   and the appearance of sharp x-ray diffraction peaks corresponding to crystalline phases over time.

247   The transformation is also accompanied by an increase in pH to approximately ~11.5.

248   XRD results show that at a given temperature, the time at which diffraction peaks appear

249   varies with Si/Fe ratio. At 80°C, diffraction peaks are already present after 1 hour in the pure

250   system (Si/Fe = 0; Fig. 4A). Diffraction peaks only begin to appear after 2 hours at Si/Fe = 0.025

251   (Fig. 4B). In addition, the time of appearance and intensities of goethite and hematite peaks vary

252   with increasing Si/Fe. For example, in Fig. 4, goethite peaks are observed along with those of

253   hematite in Si/Fe = 0 after 1 hour, suggesting that goethite and hematite may have begun

254   crystallizing simultaneously. At Si/Fe = 0.025, the (101) peak of goethite at ~24° 2θ (the most

255   intense observed in this study) only begins to appear faintly after 6 hours, while the first appearance

10

256   of hematite peaks is confirmed in the sample after 4 hours. These observations suggest that

257   crystallization becomes increasingly delayed with increasing amounts of Si, with goethite being

258   delayed to a higher degree than hematite. Decreasing temperatures result in a later appearance of

259   diffraction peaks. For example, while in Si/Fe = 0 diffraction peaks of hematite and goethite are

260   observed after 1 hour at 80°C (Fig. 4), peaks begin to be observed after 3 hours at 50°C

261   (Supplementary Information, Fig. S1).

262   Results of the Rietveld refinement show χ^2 values and R factors of less than 10 and 1,

263   respectively (Supplementary Information, Table S1), indicating the good quality of fits. In Si/Fe = 0,

264   amorphous content calculation using equation (2) shows that the ferrihydrite is completely

265   consumed after 2 hours. This coincides with the time at which the pH stabilizes and the distinct

266   color change of the sample from dark brown to deep red, indicating the completion of the

267   transformation (Supplementary Information, Fig. S2). Although there is considerable uncertainty in

268   the amorphous content calculated from equation (2), particularly at low ferrihydrite contents due to

269   the low proportion of internal standard (Westphal et al, 2009), the correspondence between the time

270   at which the pH stabilizes and the time at which the calculated ferrihydrite content drops to 0 wt. %

271   supports the accuracy of the calculated values. On the other hand, for Si/Fe = 0.025, the ferrihydrite

272   does not disappear until after 10 hours. This is consistent with the increase in the percentage of

273   residual ferrihydrite after 2 hours of heating with increasing Si/Fe ratios (Fig. 5A). This indicates

274   that the overall conversion of ferrihydrite to more crystalline phases is retarded in the presence of

275   increasing amounts of Si.

276   Depending on the Si/Fe ratio and temperature, the relative proportions of goethite and

277   hematite in the final crystalline products also vary. As seen in Fig. 4, both goethite and hematite are

278   present in the pure system at 80°C, with the intensities of hematite peaks being higher compared to

279   those of goethite. At higher Si/Fe ratios, the intensities of hematite increase while those of goethite

280   decrease, becoming negligibly low at Si/Fe = 0.025. The results of the Rietveld refinement show

281   that the percentage of goethite decreases from ~22 wt. % in Si/Fe = 0 to ~0 wt. % in Si/Fe = 0.025,

282   while that of hematite increases from ~78 wt. % to ~100 wt. % (Fig. 5B). With increasing

283   temperatures, the percentage of hematite tends to increase at a given Si/Fe. For example, in Si/Fe =

284   0, hematite percentage increases from ~26 wt. % at 50°C to ~78 wt. % at 80°C.

285   Plots of the reaction progress parameter α (normalized percentages) for goethite and

286   hematite as a function of time show that crystallization proceeds by an initial rapid increase

287   followed by a plateau (Fig. 6). Fitting the time-resolved reaction progress data with the JMAK

288   model yielded characteristic S-shaped curves. Best fits to the data were achieved at different n

289   values. For example, in Si/Fe = 0, both hematite and goethite data can be fitted with n values at an

290   average of 1.07 and 1.11, respectively. The n values tend to increase with increasing Si/Fe. For

291   example, in Si/Fe = 0.025, the n values for both hematite and goethite increase to an average of 1.70

292   and 1.47, respectively (Table 1). In general, induction time t_0 values for both goethite and hematite

293   decrease with increasing temperature, indicating that nucleation occurs earlier. Increasing Si

294   concentrations generally result in an increase in the induction time for both goethite and hematite,

295   indicating that Si delays the nucleation of both goethite and hematite (Fig. 7).

296   Fitting results showed that the crystallization rates for both goethite and hematite exhibit

297   temperature dependence at a given Si/Fe, with rates increasing with increasing temperatures. With

298   increasing Si/Fe, the crystallization rates for both goethite and hematite exhibit a decreasing trend,

299   indicating that the presence of Si also inhibits the crystallization of crystalline phases as well as

300   ferrihydrite transformation. Plots of ln k vs. 1/T exhibit linear curves for all systems (Fig. 8),

301   indicating that similar crystallization mechanisms operate within the temperature range studied.

302   Apparent activation energy of crystallization $E_{a(cryst)}$ calculated using the Arrhenius equation for

303   both goethite and hematite exhibit dependence on the concentration of Si (Fig. 9). The $E_{a(cryst)}$ of

304   hematite increases from ~70.3 kJ/mol in the silica-free system to ~117.8 kJ/mol at Si/Fe = 0.025,

305   while that of goethite increases from ~68.7 kJ/mol to ~168.6 kJ/mol in the same range. Since the

306   value of $E_{a(cryst)}$ derived using the JMAK model represents contribution from both nucleation and

307   crystal growth (Lasaga, 1998), the increase in this value with increasing Si indicates an overall

12

retardation effect of Si on the crystallization for both goethite and hematite. In addition, the difference between $E_{a(cryst)}$ for hematite and goethite become larger with increasing Si/Fe, with goethite increasing more drastically than hematite. This may suggest that Si retards goethite crystallization more effectively than hematite.

TEM observation of crystalline products from 70°C showed that in the absence of Si (Si/Fe = 0, 8 hours), goethite and hematite exhibit lath and disc-shaped morphologies, respectively and grow independently from each other (Fig. 10A). To index their reflections in the diffraction patterns and in other discussions in this paper, the space groups of rhombohedral $R\ c$ and orthorhombic $Pnma$ were used for hematite and goethite, respectively. In the presence of Si (Si/Fe = 0.025) (Fig. 10B), the final reaction products (at 48 hours) are dominated by ellipsoidal crystals. These ellipsoidal crystals are identified to be hematite elongated along the c axis (Fig. 10C). Measured average particle sizes of hematite show that these ellipsoidal particles are larger (length ~320 nm, diameter ~120 nm) than the disc-shaped hematite crystals (diameter ~120 nm, thickness ~60 nm), indicating that Si modifies the crystal growth behavior of hematite (Supplementary Information, Table S2). Lath-shaped crystals with sharply terminated facets, which were overgrown epitaxially on the ellipsoidal hematite crystals, are also observed, though they are not present in significant volume fractions compared to hematite. Electron diffraction patterns were used to identify these crystals as goethite (Fig. 10D), indicating that Si likewise influences goethite growth behavior.

A STEM-ADF image and the corresponding STEM-EDS elemental map of crystals formed in the presence of Si (Si/Fe = 0.025, 48 hours) show the distribution of Si in both hematite and goethite crystals (Fig. 10E, F). The ADF signal is roughly proportional to specimen thickness, so that it can be used to examine thickness variation, surface roughness or void distribution. The ellipsoidal hematite crystal has a rough surface with voids of several to a few tens of nanometers, while the goethite crystal has a smooth and flat surface. In addition, the goethite crystal cuts through the hematite crystal, suggesting that goethite grew after the hematite formed. The Si map shows that

13

334   goethite and hematite both contain Si, with concentrations of up to ~3.0 wt. %. Si appears to be

335   present both on the surface and inside the hematite and goethite crystals, since the Si intensity

336   distributions are correlated with the crystal thickness, although it is difficult to assess to which site

337   Si is bound.

338

339   **Discussion**

I. Characteristics of Precipitates Prior to Heating

341

342   XRD results indicate that the Si/Fe of the precipitating solution does not influence the

343   mineralogy of the initially precipitated products. Rapid hydrolysis of the Fe(III) in solution due to

344   the addition of NaOH resulted in the co-precipitation of Si and Fe into poorly ordered ferrihydrite.

345   While the FTIR data show that Si became closely associated with the ferrihydrite via the formation

346   of Si-O-Fe groups, it is not clear if Si is incorporated into the structure of ferrihydrite. However,

347   recent studies have shown that Si occurs mostly on the surface (e.g. Seehra et al., 2004; Dyer et al.,

348   2010, 2012; Cismasu et al., 2014). Detailed IR studies of adsorbed Si on ferrihydrite surfaces show

349   the formation of bidentate surface complexes composed of monomeric silicate species at low Si

350   loadings similar to the concentrations used in this study (Swedlund et al., 2009). Formation of these

351   Si surface complexes results in a net release of protons that decreases the positive charge on the

352   surface (Hiemstra et al., 2007). This is consistent with the changes in the zeta potential observed

353   with increasing Si/Fe (Fig. 3). At higher Si loadings, the surface charge is expected to become more

354   negative, as the Si polymerizes and creates more acidic surface complexes (Swedlund et al., 2010).

355

356   **II. Effects of Si on Goethite Crystallization**

357

358   The apparent activation energy for crystallization of goethite in the pure system (Si/Fe = 0)

359   can be compared with available literature data to determine its crystallization mechanism. There are

14

360   no published data on its $E_{a(cryst)}$ at pH 10, as most crystallization studies were conducted at higher

361   pH (>11). However, a study (Yee et al., 2006) extrapolated $E_{a(cryst)}$ for goethite obtained at pH 11.7,

362   12.0 (Nagano et al., 1994), 13.2 (Davidson et al., 2008) and 13.7 (Shaw et al., 2005) to neutral pH

363   and obtained a value of ~94 kJ/mol at pH 7. Following this extrapolation, the predicted value of

364    $E_{a(cryst)}$ for goethite at pH 10 would fall at approximately ~68 kJ/mol, which is in good agreement

365   with that of Si/Fe = 0 calculated in this study (~68.7 kJ/mol). Under alkaline conditions, goethite is

366   thought to form via the direct precipitation of Fe(III) from solution (Schwertmann and Murad,

367   1983). The calculated $E_{a(cryst)}$ value for goethite crystallization is consistent with apparent activation

368   energies associated with dissolution and precipitation reactions in minerals, which typically range

369   from ~35 to ~65 kJ/mol or as high as ~150 kJ/mol (Lasaga, 1998). Following this mechanism,

370   goethite crystallization would require the dissolution of the ferrihydrite precursor to supply Fe(III)

371   into solution. This is then followed by the formation of goethite nuclei in solution and the growth of

372   these nuclei by the incorporation of $Fe(OH)_4^-$ from solution. The crystallization of goethite from

373   ferrihydrite is known to follow a first-order reaction mechanism, with the crystallization rate

374   dependent on the amount of remaining ferrihydrite in the system (Schwertmann and Murad, 1983;

375   Shaw et al., 2005). The average n value of 1.11, derived from fitting the goethite crystallization data

376   at Si/Fe = 0, is consistent with this interpretation.

377   The observed increase in $E_{a(cryst)}$ (and decrease in crystallization rate) with increasing Si/Fe

378   (Fig. 9) is consistent with the inhibition of goethite crystallization by Si. This is in line with

379   previous observations of ferrihydrite transformation in the presence of Si (Cornell et al., 1987).

380   Given the mechanism of goethite crystallization, this inhibition may be due to a suppression of

381   either nucleation or crystal growth or both. Previous studies on the sorption of inorganic ligands

382   such as PO_4^{3-} and SO_4^- anions have shown that these ligands form inner-sphere complexes on the

383   surface of ferrihydrite, passivating it against dissolution and limiting the supply of Fe(III) into the

384   solution (Kandori et al., 1992; Biber et al., 1994; Barron et al., 1997; Shaw et al., 2005; Davidson et

385   al., 2008; Zhu et al., 2014). Similarly, the sorption of Si on ferrihydrite surfaces could retard the

15

386   nucleation and growth of goethite by inhibiting the dissolution of ferrihydrite. The retardation of

387   goethite nucleation is supported by the observed increase in induction time t_0 with increasing Si

388   (Fig. 7). Although the value of induction time is a complex product of a number of dynamic

389   processes occurring during nucleation, it can be generalized as being proportional to the inverse of

390   the nucleation rate (Mullin, 2001). Increasing Si, therefore, results in a decrease in nucleation rate.

391   Furthermore, dissolution of ferrihydrite (though limited), also likely releases Si back into solution,

392   where it may form complexes with Fe(III) ions, limiting their availability to participate in goethite

393   nucleation and growth (Cismasu et al., 2014).

394   Apart from delaying the timing of goethite nucleation, Si also influences the nucleation

395   mechanism. The epitaxial growth of goethite on hematite substrates, observed in the TEM images

396   (Fig. 10B), suggests that goethite does not grow homogeneously directly from solution. Previous

397   studies on goethite grown in the presence of PO_4^{3-} (e.g. Barron et al., 1997; Shaw et al., 2005)

398   showed a similar behavior. These studies proposed that the limited supply of Fe(III) into the

399   solution due to the reduced solubility of ferrihydrite, which is in turn due to the sorption of foreign

400   anions, inhibits the homogeneous nucleation of goethite in solution and promotes its nucleation on

401   the surface of hematite crystals.

402   Another possible effect of Si on goethite crystallization is the poisoning of goethite growth

403   sites by preferential Si sorption on goethite surfaces. Lath-shaped goethite crystals grown in the

404   absence of Si are typically elongated along the *c* axis (Cornell and Giovanoli, 1985), similar to the

405   goethite crystals observed in this study (Fig. 10A). However, the goethite crystals overgrown on

406   hematite appear to be elongated along the *b* axis, while growth along the *c* axis appears to be

407   stunted (Fig. 10D). Due to the higher concentration of hydroxyl groups on the {021} plane relative

408   to other planes on goethite (Barron and Torrent, 1996), foreign anions preferentially adsorb on this

409   plane, which may inhibit crystal growth along directions roughly perpendicular to this plane.

410   Sorption of Si on this plane could result in retarded growth along the *c* axis, while forcing the

411   goethite to grow along the *a* and *b* axes (Glasauer et al., 1999). This may explain the sharply

16

412 terminated plane perpendicular to the *c* axis and the elongation of the goethite crystal along the *b*

413 axis observed in the TEM images. Due to lower concentrations of hydroxyl groups on planes

414 perpendicular to the *a* and *b* axes (e.g. {100}, {110}, {010}; Barron and Torrent, 1996), overall

415 crystal growth rate may be retarded compared to the pure system. Thus, apart from retarding

416 goethite nucleation by limiting the supply of soluble Fe(III) species, Si may also retard goethite

417 crystal growth by poisoning its growth surfaces.

418

419 **III. Effects of Si on Hematite Crystallization**

420

421 The calculated $E_{a(cryst)}$ for hematite at pH 10 (~70.3 kJ/mol) is comparable to published

422 values obtained at pH 10.7 (~69 kJ/mol; Shaw et al., 2005) and pH 10 (~65 kJ/mol; Das et al.,

423 2011a). In contrast to goethite, hematite is thought to form via aggregation and dehydroxylation of

424 ferrihydrite (Cornell and Schwertmann, 2003). The aggregation and dehydration process is then

425 followed by a solid-state internal transformation process (Schwertmann and Murad, 1983).

426 However, the calculated $E_{a(cryst)}$ value is significantly lower than apparent activation energies

427 typically associated with solid-state transformation processes, which range from ~85 to ~400 kJ/mol

428 (Lasaga, 1998). Spectroscopic studies (Manceau and Drits, 1993) have noted that the transformation

429 of ferrihydrite to hematite involves the movement of O atoms to different sites, necessitating the

430 partial dissolution of the ferrihydrite framework. Later isotopic studies (Bao and Koch, 1999)

431 similarly suggested that partial dissolution of the ferrihydrite occurs alongside solid-state internal

432 rearrangement processes, although the extent to which this occurs is not clear. If correct, these

433 studies suggest that partial dissolution could lower the activation barrier to hematite crystallization

434 than if only solid-state rearrangement is involved. If partial dissolution is involved, then some

435 Fe(III) is released into solution, which could contribute to the growth of hematite crystals by

436 ripening. Furthermore, ferrihydrite to hematite transformation is thought to follow a first-order

17

437   kinetic reaction similar to goethite (Fischer and Schwertmann, 1975). The average n value derived

438   from the fitting is consistent with this interpretation.

439   The observed increase in hematite percentage relative to goethite in this study (Fig. 5) is

440   consistent with a previous study showing that the presence of Si 'promotes' the formation of

441   hematite at the expense of goethite (Cornell et al., 1987). In the previous study, this 'promotion'

442   was explained in terms of the combined effect of Si and salts in the solution. However, in the

443   present study, since Si was introduced as TEOS, variations in the concentration of Si did not

444   introduce changes in electrolyte concentrations. Thus, the salt concentrations in all of the samples

445   are approximately constant. Instead, apparent promotion of hematite relative to goethite may be

446   understood in terms of the competitive processes that control crystallization. The critical process in

447   hematite crystallization involves the aggregation of ferrihydrite. The aggregation rate is dependent

448   on the particle concentration based on the equation:

449
$$\frac{dN}{dt} = -k_a N_i^2 \quad (6)$$

450   where N_i is the initial concentration of particles and k_a is the rate constant for particle transport

451   (Stumm and Morgan, 1996). This indicates that the number of particles in a system decreases faster

452   (i.e. aggregation is favored) with higher concentrations of initial particles. If ferrihydrite dissolution

453   is suppressed by the sorption of Si, the concentration of ferrihydrite particles that become available

454   for aggregation increases, leading to the formation of hematite. Thus, there is an indirect promotion

455   effect of Si on hematite crystallization.

456   However, the increase in the $E_{a(cryst)}$ for hematite with increasing Si (Fig. 9) indicates that

457   hematite is likewise inhibited. This may indicate that hematite nucleation and crystal growth may be

458   more directly affected by the presence of Si. Aggregation of ferrihydrite, for example, may be

459   inhibited by ligands that introduce electrostatic repulsion. Aggregation of ferrihydrite is favored at

460   near neutral to slightly alkaline pH conditions, close to the pH_{pzc} of ferrihydrite (Cornell and

461   Schwertmann, 2003). At pH 10, the charge on the ferrihydrite is slightly negative, due to the

462   presence of OH^- surface groups. However, as seen from the zeta potential data of the initial

18

463 precipitates, the surface charge of ferrihydrite becomes more negative with increasing Si/Fe (Fig. 3).

464 The increasing negative charge on the surface of ferrihydrite may inhibit the aggregation of

465 ferrihydrite, resulting in the retardation of hematite nucleation. This may explain the increase in

466 induction time t_0 with increasing Si (Fig. 7).

467 The growth of hematite crystals may also be retarded by the presence of Si on their surfaces.

468 Previous studies on the sorption inorganic anions such as sulfate (Sugimoto and Wang, 1998) and

469 phosphate (Jia et al., 2005; Jia et al., 2008) and organic compounds such as amino acids (Kandori et

470 al., 2006) and ascorbic acids (Tan et al., 2014) on hematite particles have shown that these

471 compounds promote the anisotropic growth of hematite. Due to higher concentrations of hydroxyl

472 groups on planes parallel to the *c* axis of hematite, the growth in a pure system proceeds more

473 readily in the in-plane direction of the {001} plane. Preferential sorption of sulfate anions, amino

474 acids and ascorbic acids on these planes restricts growth in the in-plane direction and forces growth

475 to proceed along the *c* axis. This shift in growth direction may be manifested as an increase in the

476 length of the *c* axis (Tan et al., 2014). In this study, unit cell parameters for hematite derived from

477 Rietveld refinement show the *c* axis increases with increasing Si/Fe (Fig. 11), which could be

478 associated with morphological change. This is confirmed by the ellipsoidal morphology and the

479 elongation along the *c* axis assumed by hematite crystals in the presence of Si (Fig. 10B,C),

480 indicating Si likewise promotes the anisotropic growth of hematite crystals. These observations are

481 consistent with the mechanism of hematite crystallization involving the partial dissolution of

482 ferrihydrite and the release Fe(III) and Si into solution. Due to the lower concentrations of hydroxyl

483 groups on planes perpendicular to the *c* axis, growth may proceed slower along this direction.

484 However, it is not clear to what extent this process contributes to the overall inhibition of hematite

485 crystallization.

486

487 **IV. Overall Role of Si in Fe(III) Mineral Crystallization**

488

489   The effects of Si on the crystallization of Fe(III) phases are summarized in Fig. 12. While it

490   is clear both goethite and hematite are inhibited by the presence of Si, the changes in the apparent

491   activation energy data with increasing Si suggest that goethite is more inhibited relative to hematite

492   (Fig. 9). As discussed in the preceding sections, Si influences different stages of the crystallization

493   process for both phases. At a given Si/Fe, goethite nucleation may be retarded by the limited supply

494   of Fe(III) due to retarded ferrihydrite dissolution, while hematite nucleation is retarded by inhibited

495   ferrihydrite aggregation. The delay in the nucleation of both phases is manifested as an increase in

496   induction time t_0 (Fig. 7). However, the delay in goethite, most evidently seen in Si/Fe = 0.025, is

497   longer relative to hematite, indicating that the inhibition of goethite nucleation is more effective

498   compared to hematite. This may be understood in terms of differences in activation energies

499   associated with dissolution and particle aggregation. An estimate of the apparent activation energy

500   for the reductive dissolution of ferrihydrite is placed at approximately ~41 kJ/mol (Erbs et al., 2010).

501   This indicates that the dissolution process itself, which involves the removal of metal centers on the

502   surface, is characterized by a relatively high activation barrier. In contrast, the activation energy

503   related to overcoming electrostatic forces against ferrihydrite aggregation is estimated at ~24 kJ/mol

504   (Shaw et al., 2005). These published values show that the activation barrier to dissolve ferrihydrite

505   is higher compared to the barrier required to aggregate ferrihydrite particles. Thus, with increasing

506   Si concentration, the ferrihydrite particles have a greater tendency to aggregate than to dissolve.

507   Assuming that the relative difference between these values is true at any given Si/Fe, this may

508   explain the greater degree of inhibition of goethite crystallization relative to hematite. However, at

509   higher degrees of Si loading, the increasingly negative surface charge of ferrihydrite particles due to

510   Si polymerization may eventually inhibit transformation even to hematite.

511   Although this study investigated very low degrees of Si loading, it may be reasonable to

512   assume that the mechanism discussed above may become more pronounced at higher concentrations

513   of Si. Average concentrations of Si in natural waters are in the range of a few tens to a few hundred

514   mg/L (Iler, 1979; Treguer et al., 1995; Gallinari et al., 2002; Cornelis et al., 2011). At higher Si

515   loading, surface coverage increases and Si polymerizes on the surfaces of oxides, forming linked

516   silanol groups (Swedlund et al., 2009). With increasing degrees of polymerization, the acidity of

517   these silanol groups also increases, imparting increasingly negative surface charges to oxide

518   surfaces (Swedlund et al., 2010). This translates to a greater degree of surface passivation and hence

519   greater degree of inhibition. This is supported by preliminary experiments conducted for this study

520   at Si/Fe $\geq$ 0.01, where samples exhibited the characteristic dark brown color of ferrihydrite even

521   after more than 1 week of heating at 70°C, indicating the absence of crystallization.

522

523   <div align="center">**Implications**</div>

524   Due to the relatively high surface area of ferrihydrite, it exhibits excellent sorption

525   properties for various hazardous elements compared to crystalline phases such as goethite, hematite

526   and lepidocrocite (Peak and Sparks, 2002; Das et al., 2013). In a broader context, in settings like

527   glass/steel interfaces in high-level waste disposal systems, mine drainages and soil environments,

528   ferrihydrite can serve as excellent sinks for potentially hazardous elements such as actinides and

529   heavy metals. However, due to its metastable nature, it readily transforms into crystalline phases,

530   creating issues about the retention or possible remobilization of elements already taken up by

531   ferrihydrite.

532   The kinetic data reported in this study may be useful in predicting the long-term behavior of

533   metastable Fe(III) phases as well as crystallization timescales of Fe(III) minerals in environments

534   where Si is present and thus, the fate of hazardous elements. Specifically, the increased persistence

535   of metastable phases is expected to provide longer-term and stable sinks for hazardous elements

536   (Fukushi et al., 2003; Das et al., 2011b). The delayed crystallization of Fe(III) phases likewise

537   delays the rate of release of these elements into the wider environment, limiting the concentration of

538   these elements in nature. In the context of radioactive waste disposal systems, a critical information

539   in building safety cases for engineered barrier systems are the time frames at which certain

540   components can be expected to play a role in retarding the migration of radionuclides (IAEA, 2012).

<div align="center">21</div>

541 Kinetic data reported in this study can be used to estimate the timescales at which Fe(III) minerals

542 will be able to serve as sinks for radionuclides released from dissolving waste packages under

543 worst-case scenarios involving oxidizing conditions.

544   This study also showed that Si modifies the transformation pathway of ferrihydrite by

545 suppressing goethite crystallization, indirectly facilitating the formation of hematite. Recent studies

546 on the fate of adsorbed elements such as U (Marshall et al., 2014), Mo and V (Brinza et al., 2015)

547 following the transformation of ferrihydrite have shown that these elements may be incorporated

548 into the structure of hematite. In addition, hematite has also been observed to have better sorption

549 capabilities for elements such as Se compared to other crystalline Fe(III) phases (Rovira et al.,

550 2008). By favoring the formation pathway of hematite, the presence of Si may potentially provide a

551 mechanism by which previously adsorbed hazardous elements can be retained even after

552 transformation.

553

563

564   **List of References**

565 Avrami, M. (1939) Kinetics of phase change I - General theory. Journal of Chemical Physics, 7(12),

566   1103-1112.

22

567   Avrami, M. (1940) Kinetics of phase change II - Transformation - time relations for random

568   distribution of nuclei. Journal of Chemical Physics, 8(2), 212.

569   Avrami, M. (1941) Granulation, phase change, and microstructure - Kinetics of phase change. III.

570   Journal of Chemical Physics, 9(2), 177-184.

571   Bao, H.M., and Koch, P.L. (1999) Oxygen isotope fractionation in ferric oxide-water systems: Low

572   temperature synthesis. Geochimica Et Cosmochimica Acta, 63(5), 599-613.

573   Bargar, J.R., Reitmeyer, R., and Davis, J.A. (1999) Spectroscopic confirmation of uranium(VI)-

574   carbonato adsorption complexes on hematite. Environmental Science & Technology, 33(14),

575   2481-2484.

576   Barron, V., Galvez, N., Hochella, M.F., Jr., Torrent, J. (1997) Epitaxial overgrowth of goethite on

577   hematite synthesized in phosphate media: A scanning force and transmission electron

578   microscopy study. American Mineralogist, 82, 1091-1100.

579   Barron, V., and Torrent, J. (1996) Surface hydroxyl configuration of various crystal faces of

580   hematite and goethite. Journal of Colloid and Interface Science, 177(2), 407-410.

581   Bazilevskaya, E., Archibald, D.D., and Martinez, C.E. (2012) Rate constants and mechanisms for

582   the crystallization of Al nano-goethite under environmentally relevant conditions.

583   Geochimica Et Cosmochimica Acta, 88, 167-182.

584   Biber, M.V., Afonso, M.D., and Stumm, W. (1994) The Coordination chemistry of weathering .4.

585   Inhibition of the dissolution of oxide minerals. Geochimica Et Cosmochimica Acta, 58(9),

586   1999-2010.

587   Brinza, L., Vu, H.P., Shaw, S., Mosselmans, J.F.W., and Benning, L.G. (2015) Effect of Mo and V

588   on the hydrothermal crystallization of hematite from ferrihydrite: An *in situ* energy

589   dispersive x-ray diffraction and x-ray absorption spectroscopy study. Crystal Growth &

590   Design, doi: 10.1021/acs.cgd.5b00173, in press.

591   Buekers, J., Amery, F., Maes, A., and Smolders, E. (2008) Long-term reactions of Ni, Zn and Cd

592   with iron oxyhydroxides depend on crystallinity and structure and on metal concentrations.

593   European Journal of Soil Science, 59(4), 706-715.

594   Cismasu, A.C., Michel, F.M., Tcaciuc, A.P., and Brown, G.E. (2014) Properties of impurity-bearing

595   ferrihydrite III. Effects of Si on the structure of 2-line ferrihydrite. Geochimica Et

596   Cosmochimica Acta, 133, 168-185.

597   Cornelis, J.T., Delvaux, B., Georg, R.B., Lucas, Y., Ranger, J., and Opfergelt, S. (2011) Tracing the

598   origin of dissolved silicon transferred from various soil-plant systems towards rivers: a

599   review. Biogeosciences, 8(1), 89-112.

600   Cornell, R.M., Giovanoli, R., and Schindler, P.W. (1987) Effect of silicate species on the

601   transformation of ferrihydrite into goethite and hematite in alkaline media. Clays and Clay

602   Minerals, 35(1), 21-28.

603   Cornell, R.M., Schwertmann, U. (2003) The Iron Oxides: Structure, Properties, Reactions,

604   Occurrences and Uses, 2nd ed., 703 p. Wiley-VCH, Weinheim.

605   Cudennec, Y., and Lecerf, A. (2006) The transformation of ferrihydrite into goethite or hematite,

606   revisited. Journal of Solid State Chemistry, 179(3), 716-722.

607   Das, S., Hendry, M.J., and Essilfie-Dughan, J. (2011a) Transformation of two-line ferrihydrite to

608   goethite and hematite as a function of pH and temperature. Environmental Science &

609   Technology, 45(1), 268-275.

610   Das, S., Hendry, M.J., and Essilfie-Dughan, J. (2011b) Effects of adsorbed arsenate on the rate of

611   transformation of 2-Line ferrihydrite at pH 10. Environmental Science & Technology,

612   45(13), 5557-5563.

613   Das, S., Hendry, M.J., and Essilfie-Dughan, J. (2013) Adsorption of selenate onto ferrihydrite,

614   goethite, and lepidocrocite under neutral pH conditions. Applied Geochemistry, 28, 185-193.

615 Davidson, L.E., Shaw, S., and Benning, L.G. (2008) The kinetics and mechanisms of

616   schwertmannite transformation to goethite and hematite under alkaline conditions. American

617   Mineralogist, 93(8-9), 1326-1337.

618 De La Torre, A.G., Bruque, S., and Aranda, M.A.G. (2001) Rietveld quantitative amorphous

619   content analysis. Journal of Applied Crystallography, 34, 196-202.

620 Doelsch, E., Stone, W.E.E., Petit, S., Masion, A., Rose, J., Bottero, J.Y., and Nahon, D. (2001)

621   Speciation and crystal chemistry of Fe(III) chloride hydrolyzed in the presence of SiO4

622   ligands. 2. Characterization of Si-Fe aggregates by FTIR and Si-29 solid-state NMR.

623   Langmuir, 17(5), 1399-1405.

624 Doelsch, E., Masion, A., Rose, J., Stone, W.E.E., Bottero, J.Y., Bertsch, P.M. (2003) Chemistry and

625   structure of colloids obtained by hydrolysis of Fe(III) in the presence of SiO_4 ligands.

626   Colloids and Surfaces A, 217, 121-128.

627 Dyer, L., Fawell, P.D., Newman, O.M.G., and Richmond, W.R. (2010) Synthesis and

628   characterisation of ferrihydrite/silica co-precipitates. Journal of Colloid and Interface

629   Science, 348(1), 65-70.

630 Dyer, L., Chapman, K.W., English, P., Saunders, M., Richmond, W.R. (2012) Insights into the

631   crystal and aggregate structure of Fe^{3+} oxide/silica co-precipitates. American Mineralogist,

632   97, 63-69.

633 Erbs, J.J., Berquo, T.S., Reinsch, B.C., Lowry, G.V., Banerjee, S.K., and Penn, R.L. (2010)

634   Reductive dissolution of arsenic-bearing ferrihydrite. Geochimica Et Cosmochimica Acta,

635   74(12), 3382-3395.

636 Fischer, W.R., and Schwertmann, U. (1975) Formation of hematite from amorphous iron (III)

637   hydroxide. Clays and Clay Minerals, 23(1), 33-37.

638 Fukushi, K., Sato, T., and Yanase, N. (2003) Solid-solution reactions in As(V) sorption by

639   schwertmannite. Environmental Science & Technology, 37(16), 3581-3586.

640   Gallinari, M., Ragueneau, O., Corrin, L., DeMaster, D.J., and Treguer, P. (2002) The importance of

641   water column processes on the dissolution properties of biogenic silica in deep-sea

642   sediments I. Solubility. Geochimica Et Cosmochimica Acta, 66(15), 2701-2717.

643   Glasauer, S., Friedl, J., and Schwertmann, U. (1999) Properties of goethites prepared under acidic

644   and basic conditions in the presence of silicate. Journal of Colloid and Interface Science,

645   216(1), 106-115.

646   Hazan, E., Sadia, Y., and Gelbstein, Y. (2013) Characterization of AISI 4340 corrosion products

647   using Raman spectroscopy. Corrosion Science, 74, 414-418.

648   Hiemstra, T., Barnett, M.O., and van Riemsdijk, W.H. (2007) Interaction of silicic acid with

649   goethite. Journal of Colloid and Interface Science, 310(1), 8-17.

650   Houston, J.R., Maxwell, R.S., and Carroll, S.A. (2009) Transformation of meta-stable calcium

651   silicate hydrates to tobermorite: reaction kinetics and molecular structure from XRD and

652   NMR spectroscopy. Geochemical Transactions, 10.

653   IAEA (2012) The Safety Case and Safety Assessment for the Disposal of Radioactive waste. IAEA

654   Safety Standards Series. International Atomic Energy Agency Technical Report, Vienna.

655   Iler, R.K. (1979) The Chemistry of Silica: Solubility, Polymerization, Colloid and Surface

656   Properties and Biochemistry of Silica, 896 p. Wiley-Interscience, New York.

657   JAEA (2007) Second Progress Report on Research and Development for TRU Waste Disposal in

658   Japan - Repository Design, Safety Assessment and Means of Implementation in the Generic

659   Phase, Japan Atomic Energy Agency Technical Report, Tokyo.

660   Jia, C.J., Sun, L.D., Yan, Z.G., You, L.P., Luo, F., Han, X.D., Pang, Y.C., Zhang, Z., and Yan, C.H.

661   (2005) Iron oxide nanotubes - Single-crystalline iron oxide nanotubes. Angewandte Chemie-

662   International Edition, 44(28), 4328-4333.

663   Jia, C.J., Sun, L.D., Luo, F., Han, X.D., Heyderman, L.J., Yan, Z.G., Yan, C.H., Zheng, K., Zhang,

664   Z., Takano, M., Hayashi, N., Eltschka, M., Klaui, M., Rudiger, U., Kasama, T., Cervera-

665   Gontard, L., Dunin-Borkowski, R.E., Tzvetkov, G., and Raabe, J. (2008) Large-scale

26

666   synthesis of single-crystalline iron oxide magnetic nanorings. Journal of the American

667   Chemical Society, 130(50), 16968-16977.

668 JNC (2000) H12: Project to establish the scientific and technical basis for HLW disposal in Japan

669   (H12 Report), Japan Nuclear Cycle Development Institute Technical Report, Tokyo.

670 Kandori, K., Uchida, S., Kataoka, S., and Ishikawa, T. (1992) Effects of silicate and phosphate ions

671   on the formation of ferric-oxide hydroxide particles. Journal of Materials Science, 27(3),

672   719-728.

673 Kandori, K., Sakai, M., Inoue, S., and Ishikawa, T. (2006) Effects of amino acids on the formation

674   of hematite particles in a forced hydrolysis reaction. Journal of Colloid and Interface

675   Science, 293(1), 108-115.

676 Karim, Z. (1984) Characteristics of ferrihydrites formed by oxidation of $FeCl_2$ solutions containing

677   different amounts of silica. Clays and Clay Minerals, 32(3), 181-184.

678 Kasama, T., Thuvander, M., Siusys, A., Gontard, L.C., Kovacs, A., Yazdi, S., Duchamp, M.,

679   Dunin-Borkowski, R.E., and Sadowski, J. (2015) Direct observation of doping incorporation

680   pathways in self-catalytic GaMnAs nanowires. Journal of Applied Physics, 118, 054302.

681 Kumazawa, K. (2002) Nitrogen fertilization and nitrate pollution in groundwater in Japan: Present

682   status and measures for sustainable agriculture. Nutrient Cycling in Agrosystems, 63, 129-

683   137.

684 Kwon, S.K., Shinoda, K., Suzuki, S., and Waseda, Y. (2007) Influence of silicon on local structure

685   and morphology of gamma-FeOOH and alpha-FeOOH particles. Corrosion Science, 49(3),

686   1513-1526.

687 Lasaga, A. (1998) Kinetic Theory in the Earth Sciences, 824 p. Princeton University Library,

688   Princeton.

689 Li, X., Nail, S.L. (2005). Kinetics of glycine crystallization during freezing of sucrose/glycine

690   excipient systems. Journal of Pharmaceutical Sciences, 94(3), 625-631.

691   Manceau, A., and Drits, V.A. (1993) Local-structure of ferrihydrite and feroxyhite by EXAFS

692   Spectroscopy. Clay Minerals, 28(2), 165-184.

693   Marshall, T.A., Morris, K., Law, G.T.W., Livens, F.R., Mosselmans, J.F.W., Bots, P., and Shaw, S.

694   (2014) Incorporation of uranium into hematite during crystallization from ferrihydrite.

695   Environmental Science & Technology, 48(7), 3724-3731.

696   Mullin, J.W. (2001) Crystallization, 4th ed., 600 p. Butterworth-Heinemann, Oxford.

697   Nagano, T., Nakashima, S., Nakayama, S., and Senoo, M. (1994) The use of color to quantify the

698   effects of pH and temperature on the crystallization kinetics of goethite under highly

699   alkaline conditions. Clays and Clay Minerals, 42(2), 226-234.

700   NUMO (2004a) Development of repository concepts for volunteer siting environments. Nuclear

701   Waste Management Organization of Japan Technical Report 04-03, Tokyo.

702   NUMO (2004b) Proceedings of the International Workshop on Bentonite-Cement Interaction in

703   Repository Environments, Nuclear Waste Management Organization of Japan Technical

704   Report, 04-05, Tokyo.

705   Peak, D., and Sparks, D.L. (2002) Mechanisms of selenate adsorption on iron oxides and

706   hydroxides. Environmental Science & Technology, 36(7), 1460-1466.

707   Refait, P., Benali, O., Abdelmoula, M., and Genin, J.M.R. (2003) Formation of 'ferric green rust'

708   and/or ferrihydrite by fast oxidation of iron(II-III) hydroxychloride green rust. Corrosion

709   Science, 45(11), 2435-2449.

710   Rovira, M., Gimenez, J., Martinez, M., Martinez-Llado, X., de Pablo, J., Marti, V., and Duro, L.

711   (2008) Sorption of selenium(IV) and selenium(VI) onto natural iron oxides: Goethite and

712   hematite. Journal of Hazardous Materials, 150(2), 279-284.

713   Russell, J.D. (1979) Infrared spectroscopy of ferrihydrite - evidence for the presence of structural

714   hydroxyl-groups. Clay Minerals, 14(2), 109-114.

715   Savage, D., Noy, D., and Mihara, M. (2002) Modelling the interaction of bentonite with

716   hyperalkaline fluids. Applied Geochemistry, 17(3), 207-223.

717 Schwertmann, U., and Murad, E. (1983) Effect of pH on the formation of goethite and hematite

718   from ferrihydrite. Clays and Clay Minerals, 31(4), 277-284.

719 Schwertmann, U., and Thalmann, H. (1976) Influence of [Fe(II)], [Si], and pH on formation of

720   lepidocrocite and ferrihydrite during oxidation of aqueous $FeCl_2$ solutions. Clay Minerals,

721   11(3), 189-200.

722 Seehra, M.S., Roy, P., Raman, A., and Manivannan, A. (2004) Structural investigations of synthetic

723   ferrihydrite nanoparticles doped with Si. Solid State Communications, 130(9), 597-601.

724 Shaw, S., Pepper, S.E., Bryan, N.D., and Livens, F.R. (2005) The kinetics and mechanisms of

725   goethite and hematite crystallization under alkaline conditions, and in the presence of

726   phosphate. American Mineralogist, 90(11-12), 1852-1860.

727 Stumm, W., Morgan, J.J. (1996) Aquatic Chemistry: Chemical Equilibria and Rates in Natural

728   Waters, 3rd ed., 1040 p. Wiley-Interscience, New York.

729 Sugimoto, T., Wang, Y.S., Itoh, H., and Muramatsu, A. (1998) Systematic control of size, shape

730   and internal structure of monodisperse alpha-Fe2O3 particles. Colloids and Surfaces a-

731   Physicochemical and Engineering Aspects, 134(3), 265-279.

732 Swedlund, P.J., Miskelly, G.M., and McQuillan, A.J. (2009) An attenuated total reflectance IR

733   study of silicic acid adsorbed onto a ferric oxyhydroxide surface. Geochimica Et

734   Cosmochimica Acta, 73(14), 4199-4214.

735 Swedlund, P.J., Miskelly, G.M., and McQuillan, A.J. (2010) Silicic acid adsorption and

736   oligomerization at the ferrihydrite-water interface: Interpretation of ATR-IR spectra based

737   on a model surface structure. Langmuir, 26(5), 3394-3401.

738 Tan, W.F., Yu, Y.T., Wang, M.X., Liu, F., and Koopal, L.K. (2014) Shape evolution synthesis of

739   monodisperse spherical, ellipsoidal, and elongated hematite (alpha-Fe_2O_3) nanoparticles

740   using ascorbic acid. Crystal Growth & Design, 14(1), 157-164.

29

741   Taylor, J.C., and Clapp, R.A. (1992) New features and advanced applications of Siroquant: A

742   personal computer XRD full profile quantitative analysis software package. Advances in X-

743   ray Analysis, 35, 49-55.

744   Treguer, P., Nelson, D.M., Vanbennekom, A.J., Demaster, D.J., Leynaert, A., and Queguiner, B.

745   (1995) The silica balance in the world ocean - a reestimate. Science, 268(5209), 375-379.

746   Vaughan, G., Brydson, R., and Brown, A. (2012) Characterisation of synthetic two-line ferrihydrite

747   by electron energy loss spectroscopy. Journal of Physics: Conference Series 371, Electron

748   Microscopy and Analysis Group Conference 2011, Birmingham.

749   Vempati, R.K., and Loeppert, R.H. (1989) Influence of structural and adsorbed Si on the

750   transformation of synthetic ferrihydrite. Clays and Clay Minerals, 37(3), 273-279.

751   Westphal, T., Füllman, T., Pöllman, H. (2009) Rietveld quantification of amorphous portions with

752   an internal standard - Mathematical consequences of the experimental approach. Powder

753   Diffraction, 24(3), 239-243.

754   Yee, N., Shaw, S., Benning, L.G., and Nguyen, T.H. (2006) The rate of ferrihydrite transformation

755   to goethite via the Fe(II) pathway. American Mineralogist, 91(1), 92-96.

756   Zhu, M., Northrup, P., Shi, C., Billinge, S.J.L., Sparks, D.L., Waychunas, G.A. (2014) Structure of

757   sulfate adsorption complexes on ferrihydrite. Environmental Science and Technology, 1 (1),

758   97-101.

759

List of Figures

761 **Figure 1**: XRD profiles of initial precipitates extracted prior to heating. At all Si/Fe, the precipitates

762 are characterized by two broad humps indicative of poorly crystalline 2-line ferrihydrite.

763 **Figure 2**: FTIR spectra of initial precipitates extracted prior to heating. In region III, an absorption

764 band corresponding to the asymmetric stretching vibrations of Fe-O-Si appears and increases in

765 intensity with increasing Si/Fe. No significant shifts can be observed in this band.

766   **Figure 3**: Zeta potential of initial precipitates measured at pH 10. The surface charge of the

767   precipitates at alkaline conditions becomes more negative with increasing Si.

768   **Figure 4**: XRD profiles for samples with different Si/Fe ratios (A. Si/Fe=0, pure system; B.

769   Si/Fe=0.025) heated at 80°C showing the crystallization over time of goethite and hematite from

770   ferrihydrite (*Fh*: Ferrihydrite; *Gt*: Goethite; *Hm*: Hematite; *C**: Corundum internal standard)

771   **Figure 5**: (A) Residual ferrihydrite after 2 hours of heating at 80°C. Error bars correspond to the

772   uncertainties propagated from the amorphous calculation formula and Rietveld refinement. (B)

773   Percentage of goethite and hematite in the final products at 80°C. Error bars correspond to

774   uncertainties derived directly from Rietveld refinement.

775   **Figure 6**: Plots of reaction progress α as a function of time for goethite and hematite at different

776   Si/Fe ratios. The solid lines represent the fits of the JMAK kinetic model.

777   **Figure 7**: Induction times for hematite and goethite at 50°C as a function of Si/Fe.

778   **Figure 8**: Arrhenius plots of (A) hematite and (B) goethite crystallization.

779   **Figure 9**: Apparent activation energy for crystallization of hematite and goethite as a function of

780   Si/Fe.

781   **Figure 10**: TEM images of final reaction products extracted at 70°C: (A) Si/Fe = 0 after 8 hours

782   and (B) Si/Fe = 0.025 after 48 hours. Electron diffraction patterns from (C) an ellipsoidal crystal as

783   shown in (B) and (D) a lath-shaped crystal overgrown on the ellipsoidal crystal, which corresponds

784   to hematite [100] and goethite [110], respectively. In (D), the forbidden reflections of 00*l* (*l*=2*n*+1)

785   and *hk*0 (2*n*+1) appear due to multiple scattering. (E) TEM image of an ellipsoidal crystal with a

786   lath-shaped overgrowth and a corresponding EDS map showing Si distribution in the two crystals.

787   (*Gt*: Goethite; *Hm*: Hematite)

788   **Figure 11**: Unit cell parameters for hematite as a function of Si/Fe ratio.

789   **Figure 12**: Summary of the effect of Si on the crystallization of goethite and hematite

790

791

31

792   **Tables**

793   **Table 1**: Summary of results of the kinetic analysis of goethite and hematite crystallization at

794   different temperatures and Si/Fe ratios.

T (°C)	Crystallization Rates k (1/hr)[a]									
	Si/Fe=0		Si/Fe=0.001		Si/Fe=0.005		Si/Fe=0.01		Si/Fe=0.025	
	Gt	Hm	Gt	Hm	Gt	Hm	Gt	Hm	Gt	Hm
50	0.204	0.253	0.0874	0.106	0.0404	0.0468	0.0243	0.0195	0.0026	0.0024
60	0.395	0.486	0.244	0.247	0.159	0.167	0.090	0.0689	0.0231	0.0135
70	0.857	1.081	0.529	0.619	0.403	0.357	0.335	0.166	0.0984	0.0236
80	1.758	2.301	1.548	1.361	1.091	0.908		0.504		0.127
n[b]	1.11	1.07	1.57	1.59	1.61	1.73	1.70	1.74	1.47	1.70
$E_{a(cryst)}$ (kJ/mol)[a]	68.7	70.3	89.1	81.4	102.8	91.8	120.9	100.9	168.6	117.8

Note(s): Gt: Goethite, Hm: Hematite
[a] Uncertainties from triplicate samples range from 3 to 5% of values reported in this table.
[b] n is reported as the average of n values from fitting at different temperatures.

795

796

797

798

799

800

801

802

803
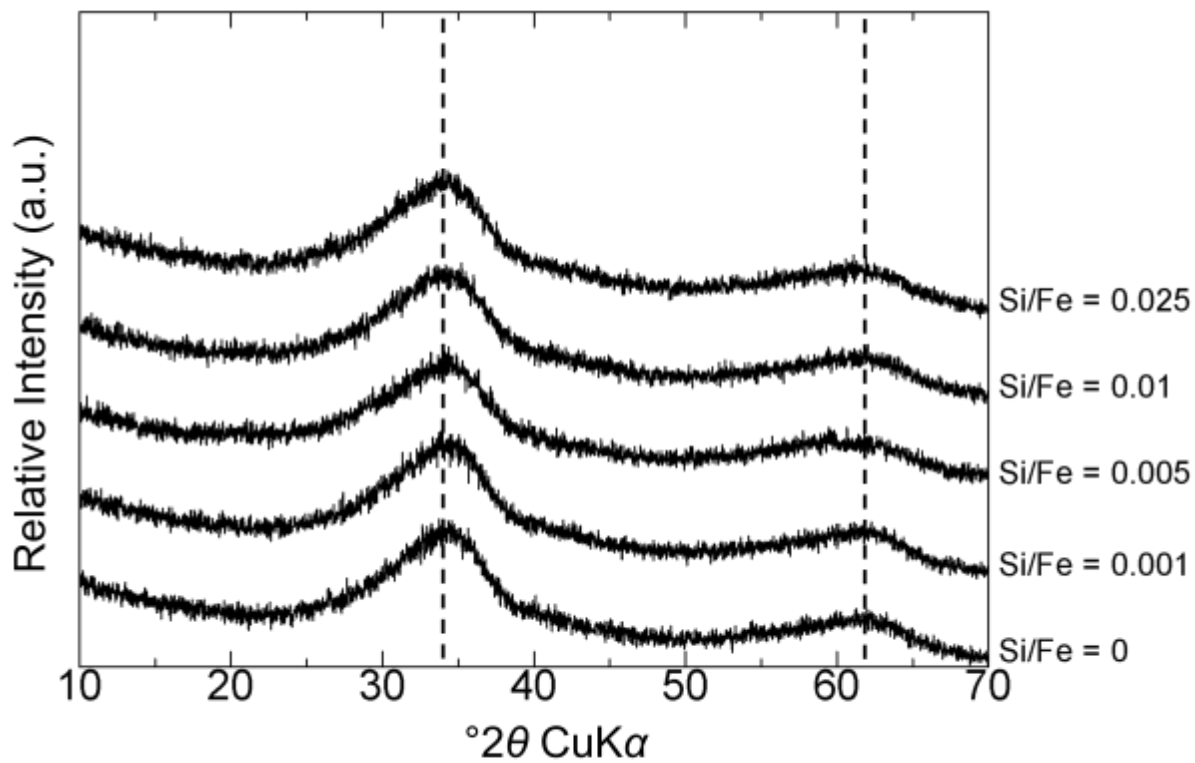
Fig. 1

804

805

806

807

808

809

810

811

812

813

814

815

816

817

818

819
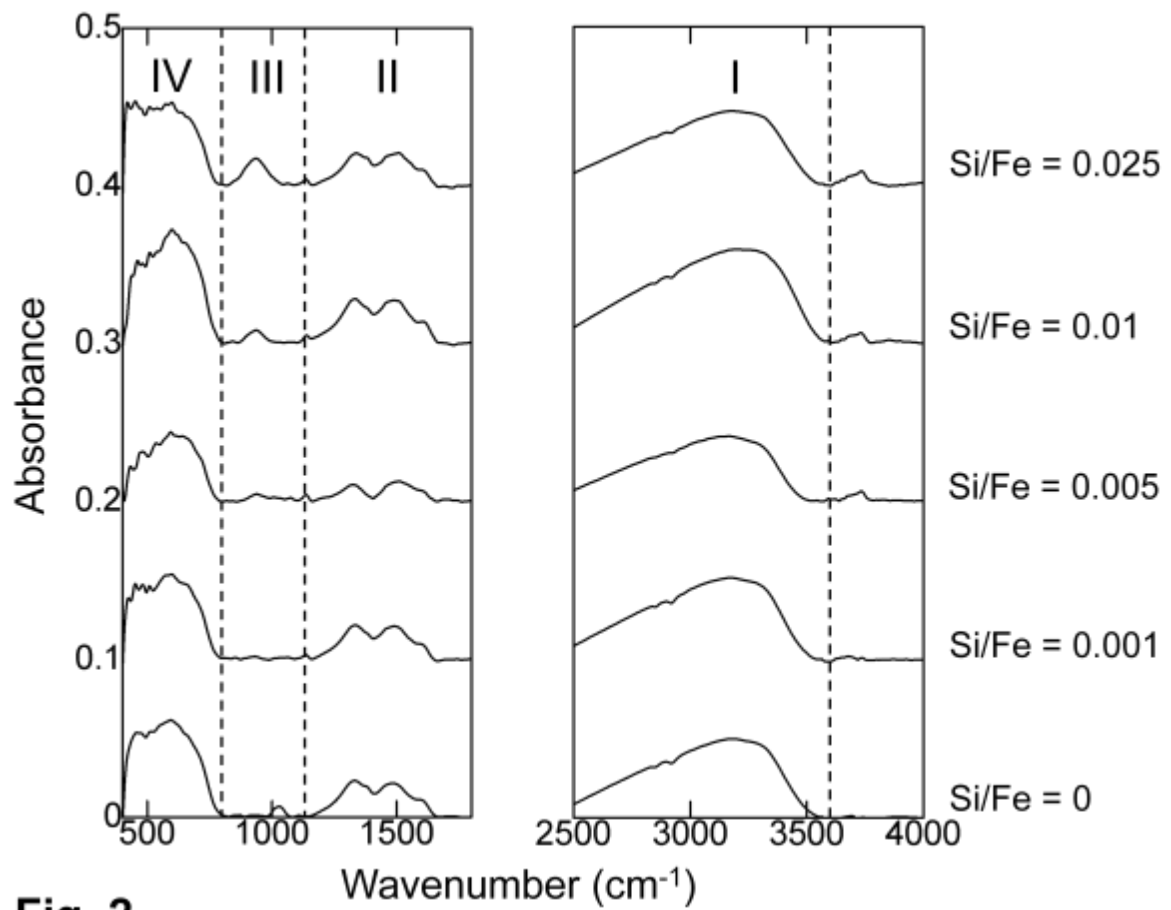
Fig. 2

820

821

822

823

824

825

826

827

828

829

830

831   '

832

833
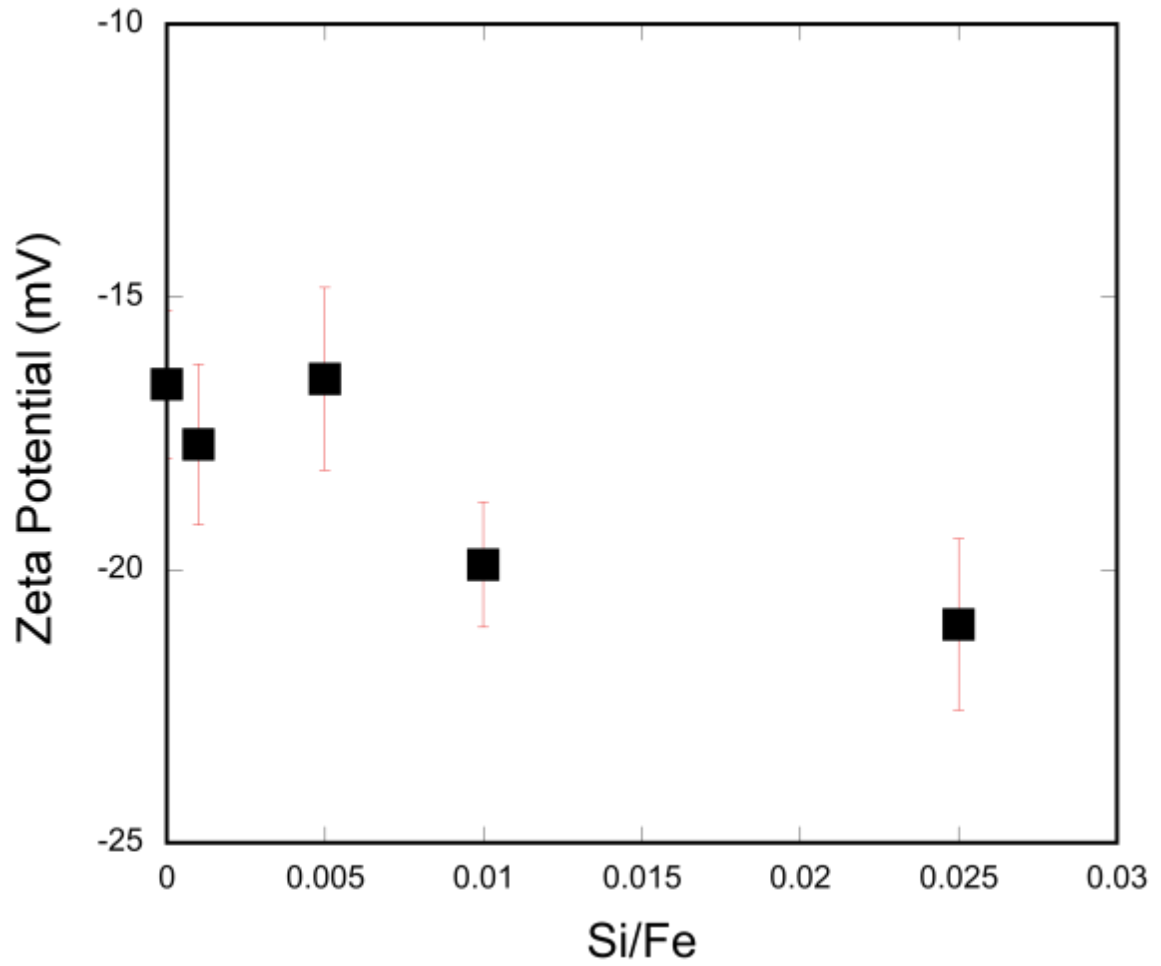
Fig. 3

834

835

836

837

838

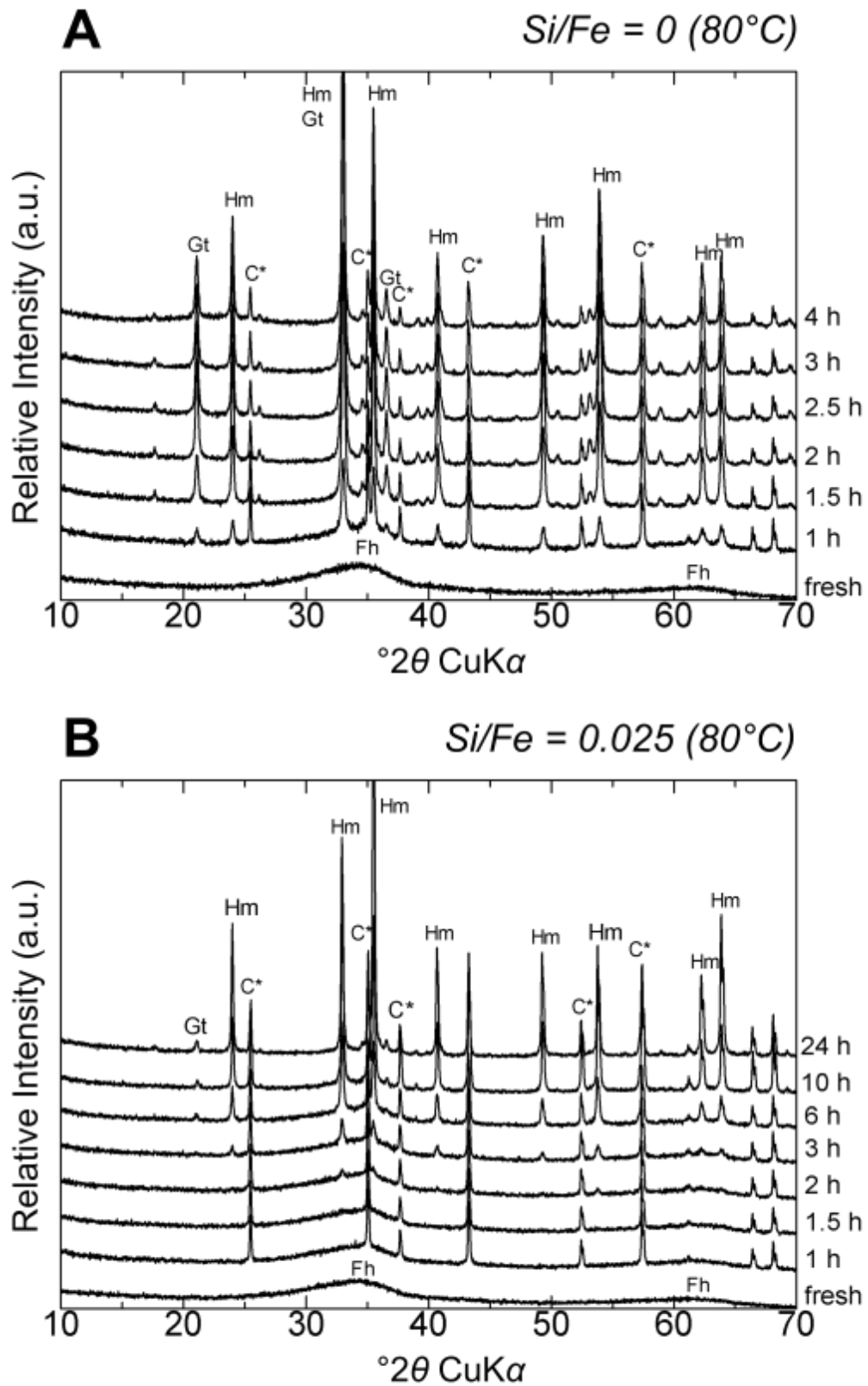839

840

841

842

843

844

845

846

847

Fig. 4
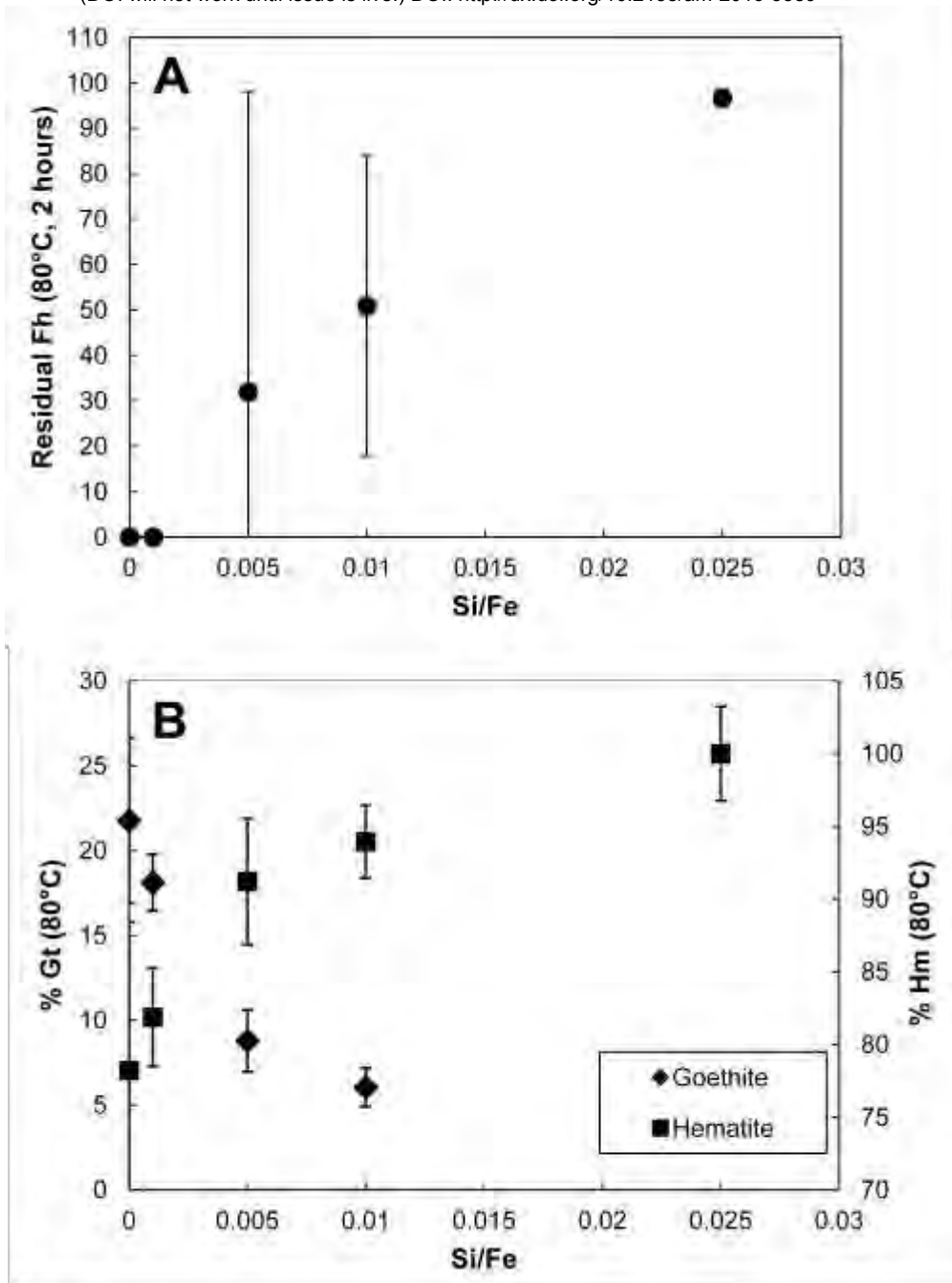
848

849

850

851

36

Fig. 5

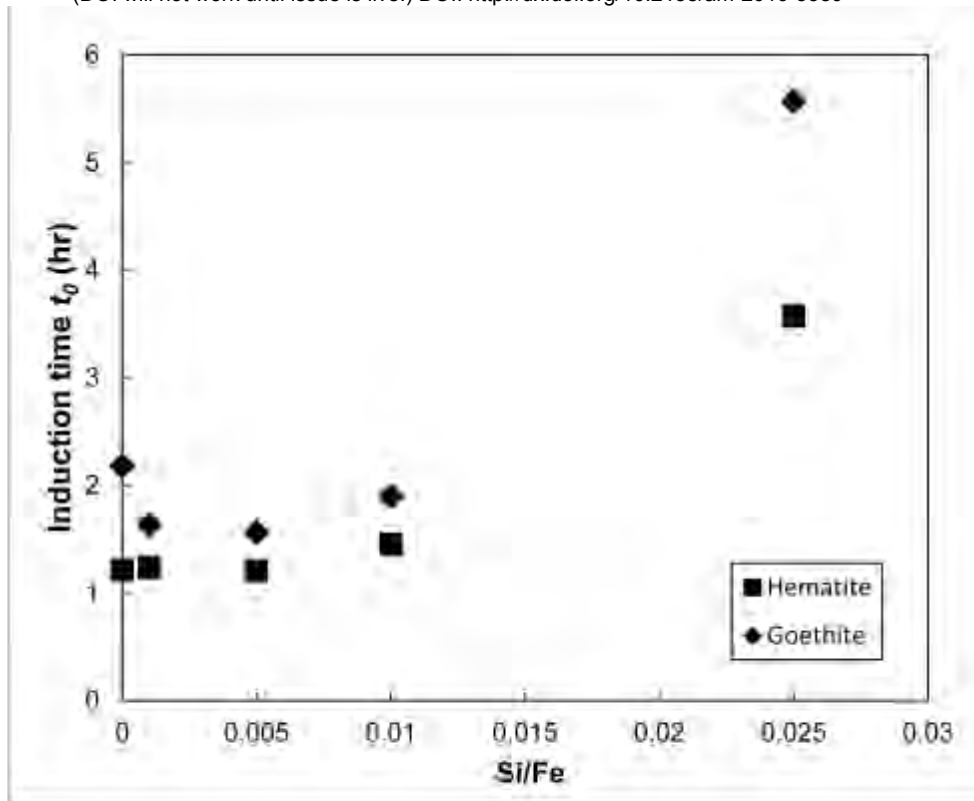852

853

854

855

856

857

858

859

860

861

862

863

38

Fig. 7

864

865

866

867
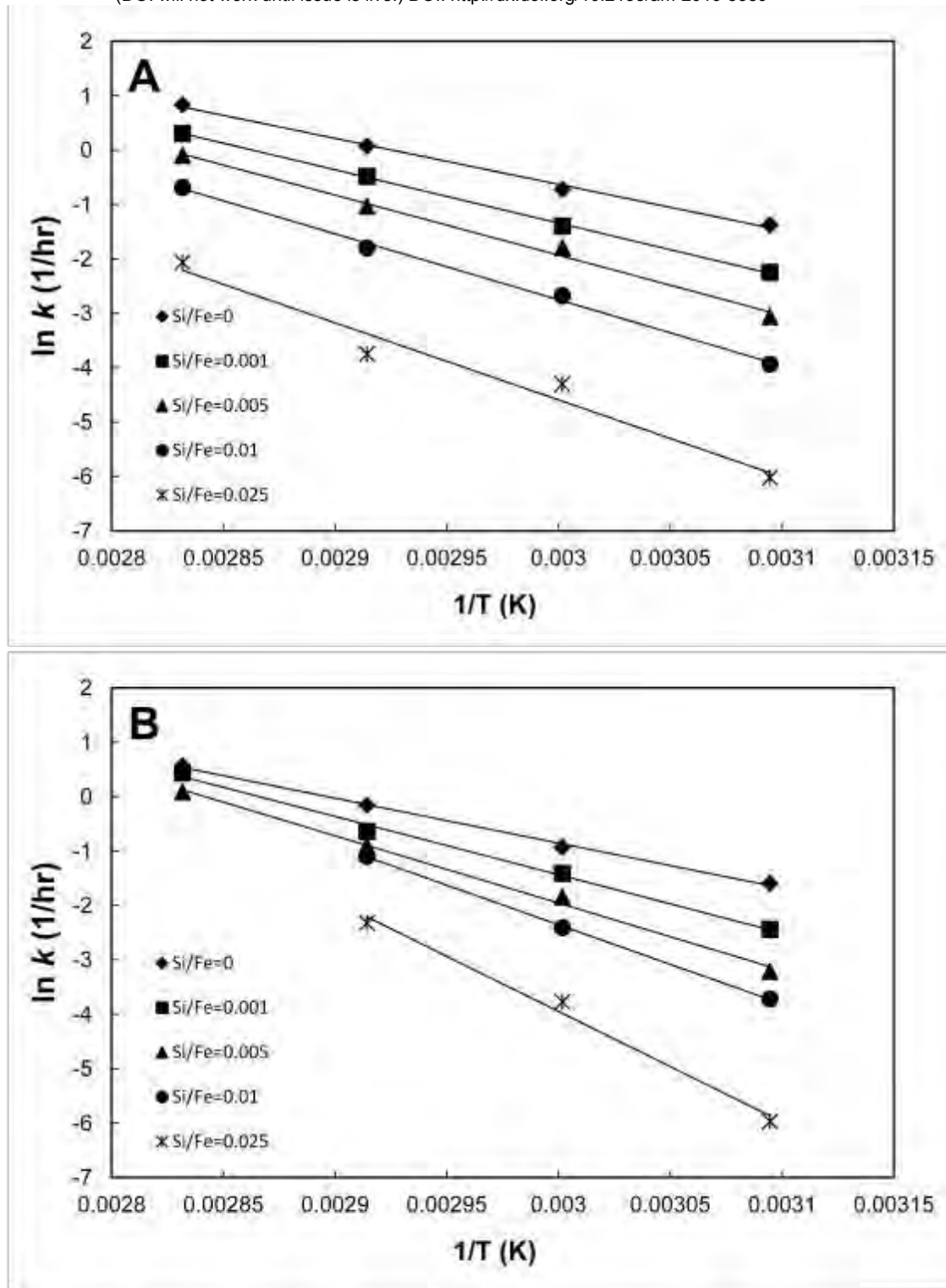
868

869

870

871

872
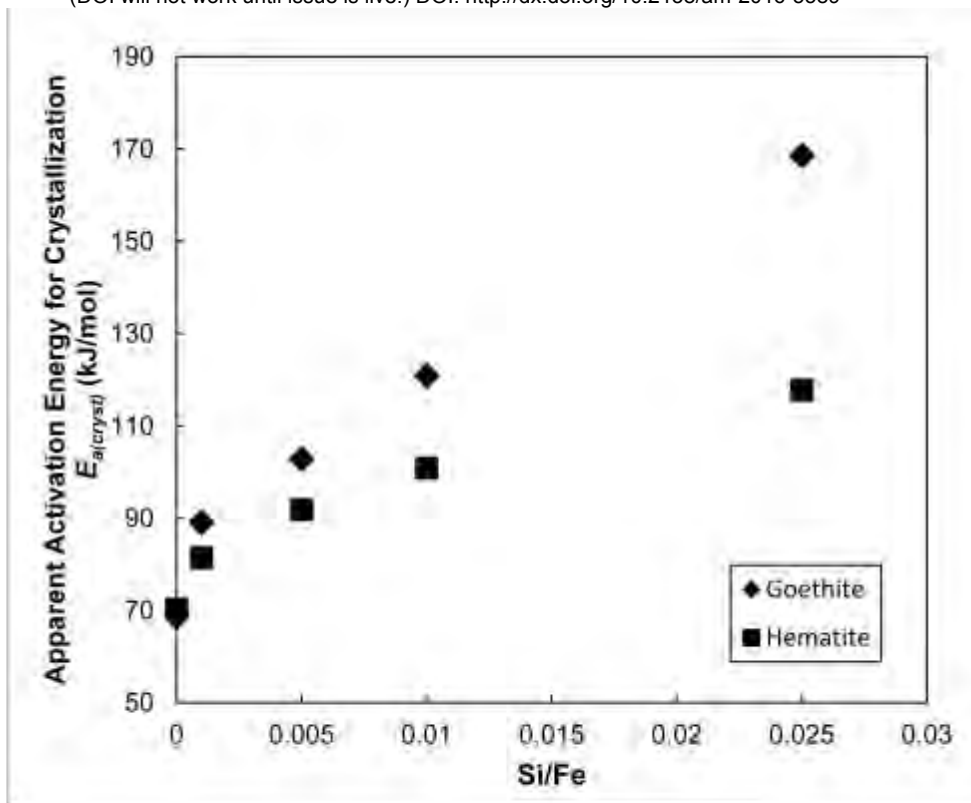
873

874

875

876

877

878

879

Fig. 8

880

881

882

883

884

40
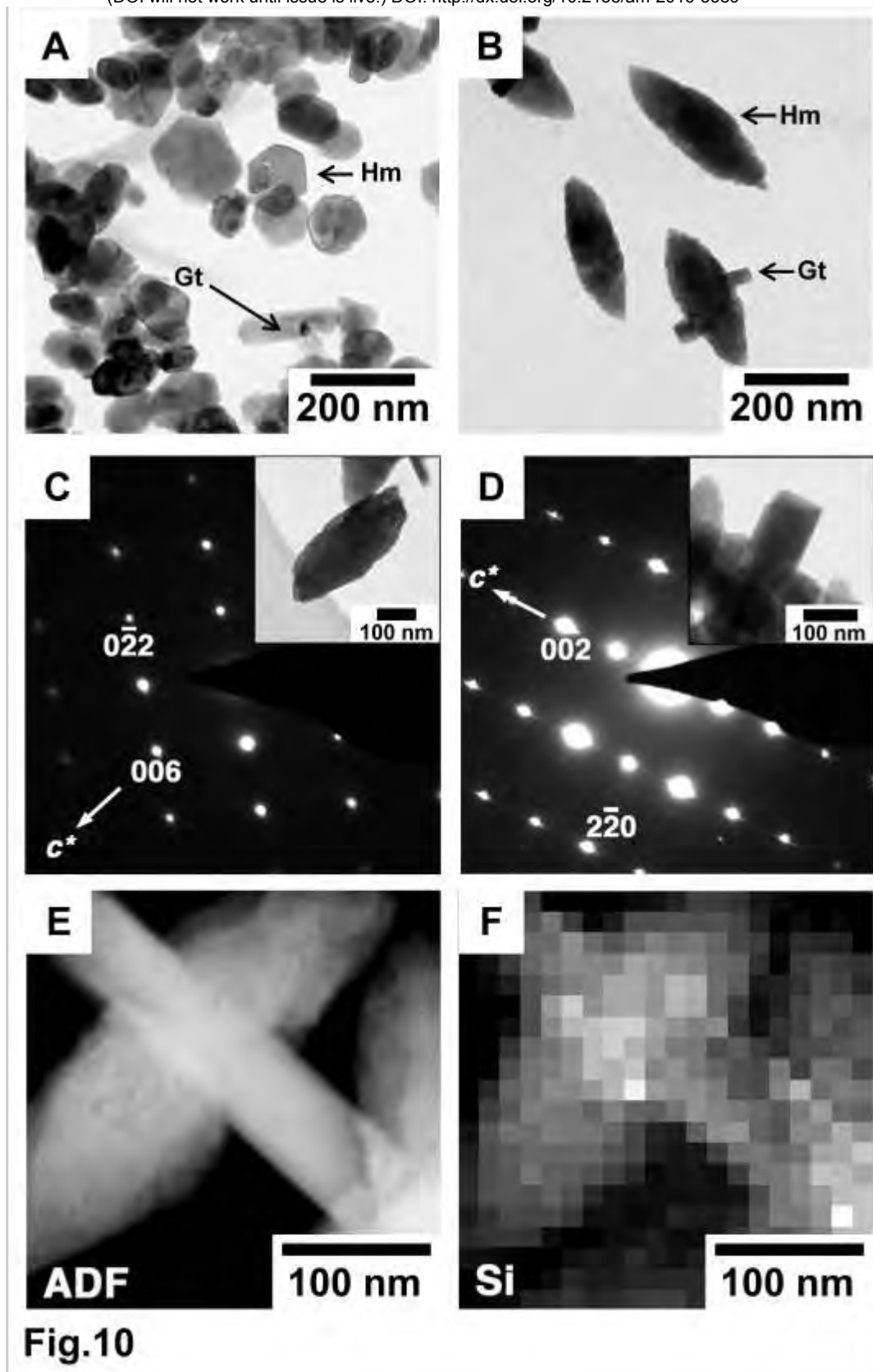
Fig. 9

885

886

887

888

889

890

891

892

893

894

895

896

897

898

899

Fig.10

900

Fig.11
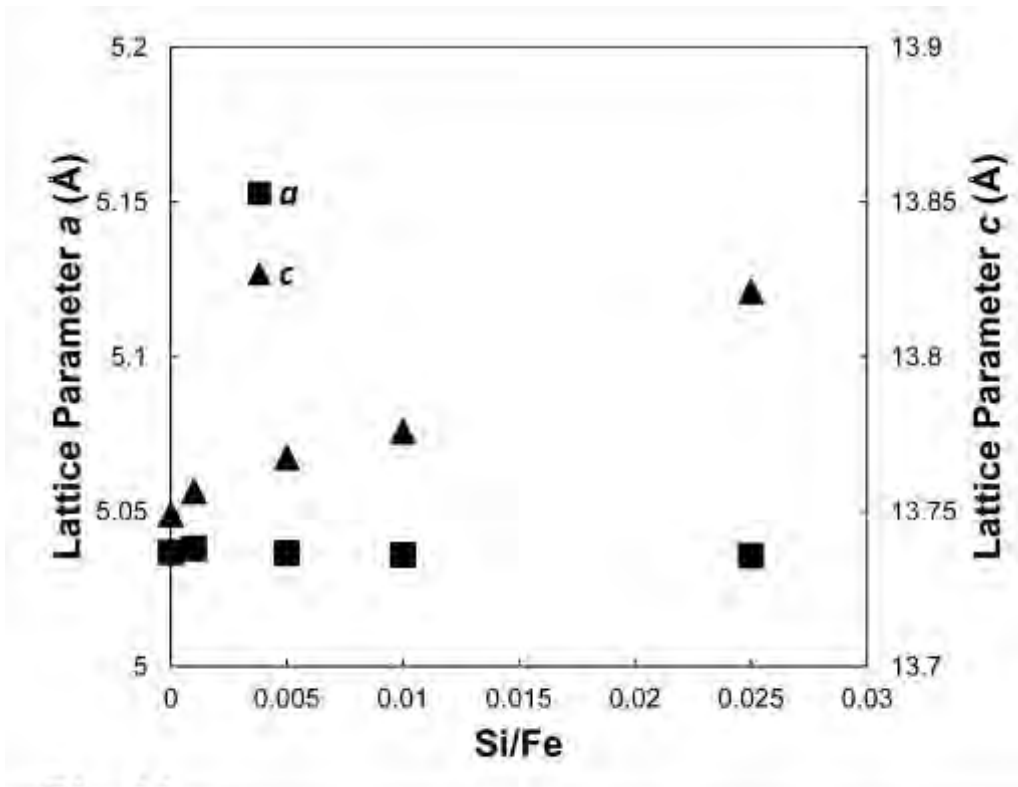
901

902

903

904

905

906
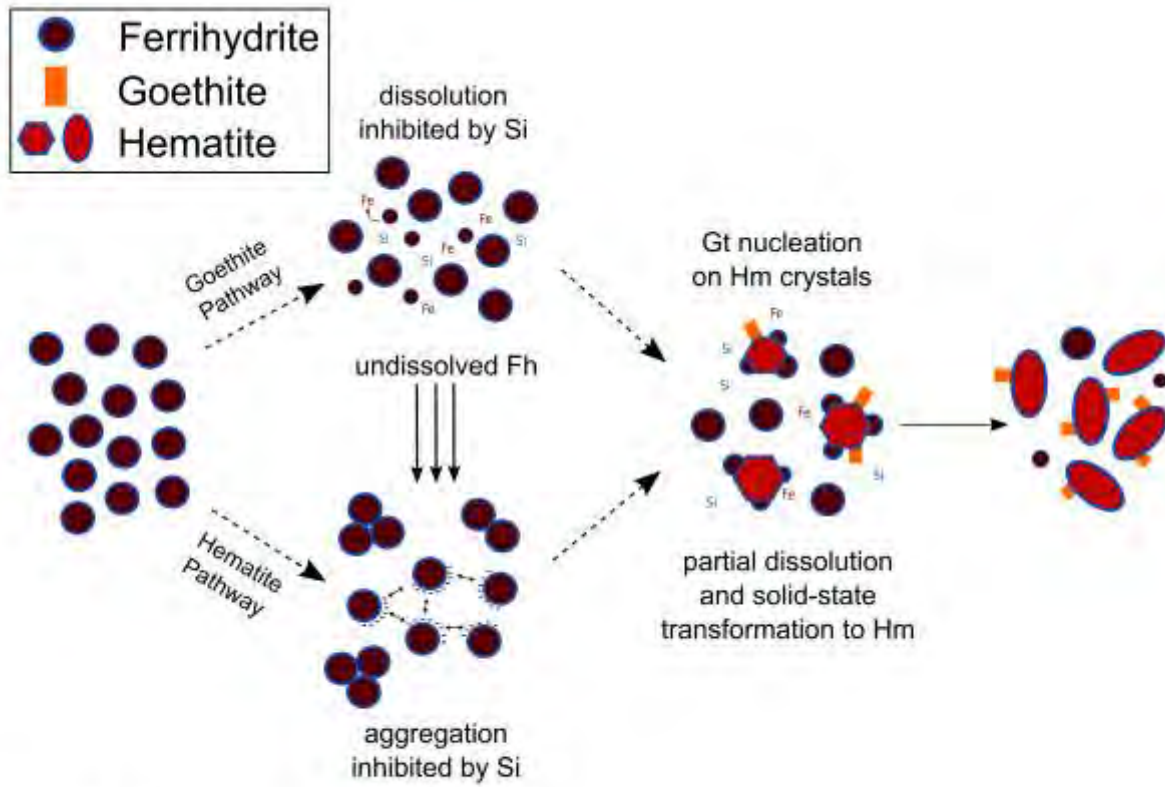
907

908

909

910

911

912

913

914

915

916

917

Fig. 12

918